PROCEEDINGS OF SCIENCE

Analysis of temporal variation of cosmic ray intensity observed with global networks of neutron monitors and muon detectors

K. Munakata[a,*], M. Kozai[b], C. Kato[a], Y. Hayashi[a], Y. Masuda[a], R. Kataoka[c,d], A. Kadokura[b,c,d], S. Miyake[e], K. Iwai[f], R. R. S. Mendonça[g], E. Echer[g], A. Dal Lago[g], M. Rockenbach[g], N. J. Schuch[h], J. V. Bageston[h], C. R. Braga[i], H. K. Al Jassar[j], M. M. Sharma[j], M. L. Duldig[k], J. E. Humble[k], I. Sabbah[l], P.-S. Mangeard[m], T. Kuwabara[m], and P. Evenson[m]

[a] *Department of Physics, Shinshu University, Matsumoto, Nagano 390-8621, Japan;*

[b] *Polar Environment Data Science Center, Joint Support-Center for Data Science Research, Research Organization of Information and Systems, Tachikawa, Tokyo 190-0014, Japan*

[c] *National Institute of Polar Research, Tachikawa, Tokyo 190-8518, Japan*

[d] *Department of Polar Science, School of Multidisciplinary Sciences, The Graduate University for Advanced Studies, SOKENDAI, Tachikawa, Tokyo 190-8518, Japan*

[e] *National Institute of Technology (KOSEN), Ibaraki College,866 Nakane, Hitachinaka-shi, Ibaraki-ken 312-8508 Japan*

[f] *Institute for Space-Earth Environmental Research, Nagoya University, Nagoya, Aichi 464-8601, Japan*

[g] *National Institute for Space Research (INPE), 12227-010 São José dos Campos, Brazil*

[h] *Southern Space Coordination, National Institute for Space Research, P.O. Box 5021-97110-970—Santa Maria, RS, Brazil*

[i] *George Mason University, 4400 University Drive, Fairfax, VA 22030, USA*

[j] *Physics Department, Kuwait University, P.O. Box 5969 Safat, 13060, Kuwait*

[k] *School of Natural Sciences, University of Tasmania, Hobart, Tasmania 7001, Australia*

[l] *Department of Laboratory Technology, College of Technological Studies, The Public Authority for Applied Education and Training, Shuwaikh, 72853, Kuwait*

[m] *Bartol Research Institute and Department of Physics and Astronomy, University of Delaware, 217 Sharp Laboratory, Newark, DE 19716, USA*

E-mail: kmuna00@shinshu-u.ac.jp

38th International Cosmic Ray Conference (ICRC2023)
26 July - 3 August, 2023
Nagoya, Japan

[*] Speaker

PoS(ICRC2023)1228

The temporal variation of cosmic ray intensity recorded by a ground-based detector includes contributions from varying cosmic ray density (or isotropic intensity) and anisotropy in space. We deduce these contributions separately and accurately, each as a function of primary cosmic ray rigidity and time, by analyzing the cosmic ray intensity observed with global networks of neutron monitors and multidirectional muon detectors altogether. In such analyses, however, we need to pay special attention to local effects including atmospheric effects which are superposed on the signal temporal variation of cosmic ray density and anisotropy. This is particularly important in analyses of the data during the "quiet period" when only small signal variation is expected. We present our analyses of the data during two sample periods in January-February and July-August, 2012, during each of which an extended cosmic ray decrease lasting for ~five days with a strong anisotropy was observed.

Introduction

The cosmic ray intensity observed at Earth dynamically changes with various timescales between a few hours and a few tens of days, in association with the arrival of solar and interplanetary disturbances, such as the interplanetary coronal mass ejections (ICMEs) with or without interplanetary (IP) shocks and corotation interaction regions (CIRs). Because of their large Larmor radii, the intensity of high-energy galactic cosmic rays (GCRs) with 1-100 GeV energies changes particularly responding to the large-scale magnetic structure passing across the Earth with the solar wind. This is why the ground-based observations using neutron monitors (NMs) and muon detectors (MDs) are important for the study of space weather.

Since the GCR intensity variation observed at a point in space consists of the combined variations due to the GCR density (omnidirectional intensity) and the anisotropy, one needs the multidirectional observations with a global network to derive these two components separately and accurately. For this purpose, worldwide network observations with NMs [1] and MDs [2] have been employed. The temporal variation of GCR density tells us the radial spatial distribution of GCR density in the GCR depleted region such as the Forbush decrease region which passes Earth being convected by the radial solar wind, while the anisotropy can tell us the three-diemnsional spatial gradient of GCR density around Earth [2]. Because a NM and a MD have typical maximum responses to GCRs with ~15 GV and ~65 GV median rigidities, respectively, we can also deduce the rigidity dependence of the variation over a wide rigidity range of 5-100 GV by analyzing NM and MD data altogether.

In an analysis using the global network data, however, we need to pay a special attention to the variation due to the "local effect" arising from the environmental variation which is generally different in each detector. In this paper, we present our sample analyses of the "extended cosmic ray decreases" observed by NMs and MDs in January-February and July-August, 2012 [3]. We particularly show the local effect seen in MD data and discuss the analysis method to eliminate its influence on the derived GCR density and anisotropy variations.

Analysis method

In this paper, we use the count rates recorded by 18 NMs and 60 directional channels of the Global Muon Detector Network (GMDN) as listed in Table 1 [4]. NM and GMDN count rates are both corrected for the atmospheric pressure effect, while GMDN count rates are also corrected for the atmospheric temperature effect by the Mass Weighted method (MSS method) using the mass-weighted temperature provided by the Global Data Assimilation System (GDAS) of the National Center for Environmental Prediction [5].

We derive the GCR density ($\xi_0^{0\ c}(t)$) and three components of the first-order anisotropy (diurnal anisotropy) vector ($\xi_1^{1\ c/s}(t)$) by best-fitting the following model function ($I_{i,j}^{fit}(t)$) to the observed data ($I_{i,j}^{obs}(t)$),

name	lat.(deg)	long.(deg)	alt.(m)	ch-no.	Pc(GV)	cph/10^4	cph error (0.01%)	Pm(GV)	alat.(deg)	along.(deg)
NM (18 directional channels)										
APTY	67.6N	33.4E	181	1	0.7	68.3	12.1	15.0	41.3	64.2
ATHN	38.0N	23.8E	260	1	8.5	20.7	22.0	22.8	3.7	82.0
BKSN	43.3N	42.7E	1700	1	5.6	42.5	15.3	16.7	-6.0	103.5
FSMT	60.0N	248.1E	203	1	0.3	100.3	10.0	15.1	33.1	269.6
INVK	68.4N	226.3E	21	1	0.3	74.9	11.6	15.1	45.2	242.1
IRK2	52.4N	100.6E	2000	1	3.6	136.1	8.6	14.0	2.8	149.6
JNG1	46.6N	8.0E	3475	1	4.5	115.2	9.3	13.5	-9.7	69.9
KERG	49.4S	70.3E	33	1	1.1	83.2	11.0	14.9	-10.9	83.0
LMKS	49.2N	20.2E	2634	1	3.8	161.9	7.9	13.5	-4.2	73.9
MXCO	19.8N	260.8E	2274	1	8.2	84.7	10.9	20.4	-11.6	327.0
NAIN	56.6N	298.3E	46	1	0.3	85.1	10.8	15.1	27.3	338.8
OULU	65.1N	25.5E	15	1	0.8	37.1	16.4	14.9	35.2	58.4
PWNK	55.0N	274.6E	53	1	0.3	86.5	10.8	15.1	26.7	307.4
SOPO	90.0S	···	2820	1	0.1	121.4	9.1	11.3	-54.7	-15.5
TERA	66.7S	140.0E	32	1	0.0	47.4	14.5	14.8	-67.5	161.3
THUL	76.5N	291.3E	26	1	0.3	47.9	14.5	15.0	67.9	322.9
TXBY	71.6N	128.8E	0	1	0.5	39.4	15.9	14.9	47.2	162.1
PSNM	18.6N	98.5E	2565	1	16.8	225.0	6.7	34.6	6.0	158.7
GMDN (60 directional channels)										
Nagoya	35.2N	137.0	77	17	8.0-12.6	17.3–285.6	5.9–24.0	58.4–106.9	64.0N–24.4S	89.1E–235.0E
Hobart	43.0S	147.3	65	13	2.5–4.0	19.9–149.3	8.2–22.4	53.1–74.0	5.0N–76.6S	122.4E–237.0E
Kuwait	29.4N	48.0	19	13	8.9–14.1	12.6–252.0	4.7–23.3	61.2–104.0	79.3N–26.1S	16.8E–136.2E
São Martinho	29.4S	306.2	488	17	7.1–14.1	4.3–257.1	6.2–48.5	54.3–98.4	33.4N–67.1S	100.6W–11.6E

Table 1. Characteristics of NMs and MDs used in this paper. From left, each column lists the detector name, geographic, longitude and altitude of detector's location, number of directional channels available from each detector, geomagnetic cutoff rigidity (P_c) for each directional channel, average hourly count rate, count rate error, median rigidity of primary GCRs (P_m), and geographic latitude and longitude of the asymptotic viewing direction outside the magnetosphere. P_m is calculated by using the response function of each detector to primary GCRs, while geographic latitude and longitude of the asymptotic viewing direction are calculated by tracing orbits of GCRs with P_m in a model magnetosphere [6].

$$I_{i,j}^{fit}(t) = \sum_{n=0}^{2}\sum_{m=0}^{n}\{\xi_n^{m\,c}(t)\left(c_{n\ i,j}^{m}\cos m\omega t_i - s_{n\ i,j}^{m}\sin m\omega t_i\right) + \xi_n^{m\,s}(t)\left(s_{n\ i,j}^{m}\cos m\omega t_i + c_{n\ i,j}^{m}\sin m\omega t_i\right)\},$$

where $I_{i,j}^{obs}(t)$ is the count rate recorded in the j-th directional channel of the i-th detector at the universal time t, $\xi_n^{m\,c}(t)$ and $\xi_n^{m\,s}(t)$ are best-fit parameters, that is, $\xi_0^{0\,c}(t)$ representing the GCR density and $\xi_1^{0\,c}(t), \xi_1^{1\,c}(t)$ and $\xi_1^{1\,s}(t)$ representing the GCR anisotropy in the GEO coordinates, t_i is the local time at the i-th detector and $\omega = \pi/12$. In the GEO coordinate system, we set the x-axis to the anti-sunward direction in the equatorial plane, the z-axis to the geographical north perpendicular to the equatorial plane, and the y-axis completing the right-handed coordinate system. Each NM has only one directional channel with $j = 1$. In this paper, we use for $I_{i,j}^{obs}(t)$ the percent deviation of hourly count rate from an average over the solar rotation period (27 days). $c_{n\ i,j}^{m}$ and $s_{n\ i,j}^{m}$ are coupling coefficients calculated using the response function and asymptotic viewing direction of each directional channel, as

$$c_{n\,i,j}^{m} = \int_{P_c}^{\infty} g_n(p)\, R(x_i, Z_j, p) P_n^m(\cos\theta_{i,j}(p)) \times \cos\{m(\phi_{i,j}(p) - \phi_i)\}\, dp / \int_{P_c}^{\infty} R(x_i, Z_j, p)\, dp$$

$$s_{n\,i,j}^{m} = \int_{P_c}^{\infty} g_n(p)\, R(x_i, Z_j, p) P_n^m(\cos\theta_{i,j}(p)) \times \sin\{m(\phi_{i,j}(p) - \phi_i)\}\, dp / \int_{P_c}^{\infty} R(x_i, Z_j, p)\, dp,$$

where $R(x_i, Z_j, p)$ is the response function of the i-th detector viewing at zenith angle Z_j and an atmospheric depth x_i to primary cosmic rays with a rigidity p, $P_n^m(\cos\theta_{i,j}(p))$ is the seminormalized spherical function by Schmidt, ϕ_i is the geographical longitude of the i-th detector, $\theta_{i,j}(p)$ and $\phi_{i,j}(p)$ are the geographical asymptotic colatitude and longitude of cosmic rays with rigidity p to be detected in the i,j directional channel, and $g_n(p)$ is the rigidity spectrum of $\xi_n^{m\,c/s}(t)$. In this study, we assume a single power-law spectrum for $g_n(p)$ as

$$g_n(p) = (p/p_r)^{\gamma_n(t)}$$

where $\gamma_n(t)$ is the power-law index. By changing $\gamma_n(t)$, each between −2.0 and +1.0 in 0.1 steps, we find $\xi_n^{m\,c/s}(t)$ and $\gamma_n(t)$ minimizing the chi-square between $I_{i,j}^{obs}(t)$ and $I_{i,j}^{fit}(t)$. More detail information of this analysis can be found in [6] in which we analyzed a significant space weather event during a few days in November 2021. In this study, we analyze two solar rotation periods in January-February and July-August, 2012, when the extended cosmic ray decreases in association with strong diurnal anisotropy were reported from the observation by the PSNM neutron monitor [3].

Results and Discussion

Figure 1 displays all data analyzed in this study. For an easy-to-see display of the common variation among detectors, we show the 24-hour trailing moving average (TMA) of hourly $I_{i,j}^{obs}(t)$ in this figure, suppressing the diurnal variation due to the anisotropy which is generally different in different viewing direction. We calculate the 24-hour TMA ($\bar{I}_{i,j}^{obs}(t)$) as

$$\bar{I}_{i,j}^{obs}(t) = \textstyle\sum_{t-23}^{t} I_{i,j}^{obs}(t)\,/24.$$

The superposed black curves in the left and right column panels display variations in January 18 - February 12 and in July 14 - August 8, respectively. The top panel shows variations observed by 18 NMs including PSNM shown by the red curve, while each of the bottom four panels displays variations observed by all directional channels in each of four muon detectors of the GMDN. It is noted that the variation amplitude in PSNM is much smaller than those of other NMs indicating the soft rigidity spectrum of the variation.

It is seen that the variations in all directional channels in each MD are quite common, while there is some differences seen between MDs. We are as yet unsure, but a possible cause of the count rate difference between MDs is the local effect, partly due to the inappropriate atmospheric temperature correction by the MSS method for some MDs. The MSS method is quite effective to correct for the large amplitude seasonal variation due to the temperature effect, but sometimes it does not work properly when there is an anomalous vertical temperature profile, such as a "stratospheric sudden warming", is observed above the local MD [7]. In this paper, we present our preliminary analysis to suppress the influence of this local effect in MD data on the best-fit parameters. Although the difference between variations in NMs are also significant as seen in the top two panels, we will investigate its correction in future work.

The top panels of Figure 2 display $\bar{I}_{i,1}^{obs}(t)$ in four vertical channels in GMDN (Nagoya in red, Hobart in blue, Kuwait in orange and São Martinho in slyblue), while the bottom five panels show the best-fit parameters at 65 GV monitored by the GMDN. From the second to the bottom, each panel shows the best-fit density ($\xi_0^{0\,c}(t)$), the amplitude of the diurnal anisotropy

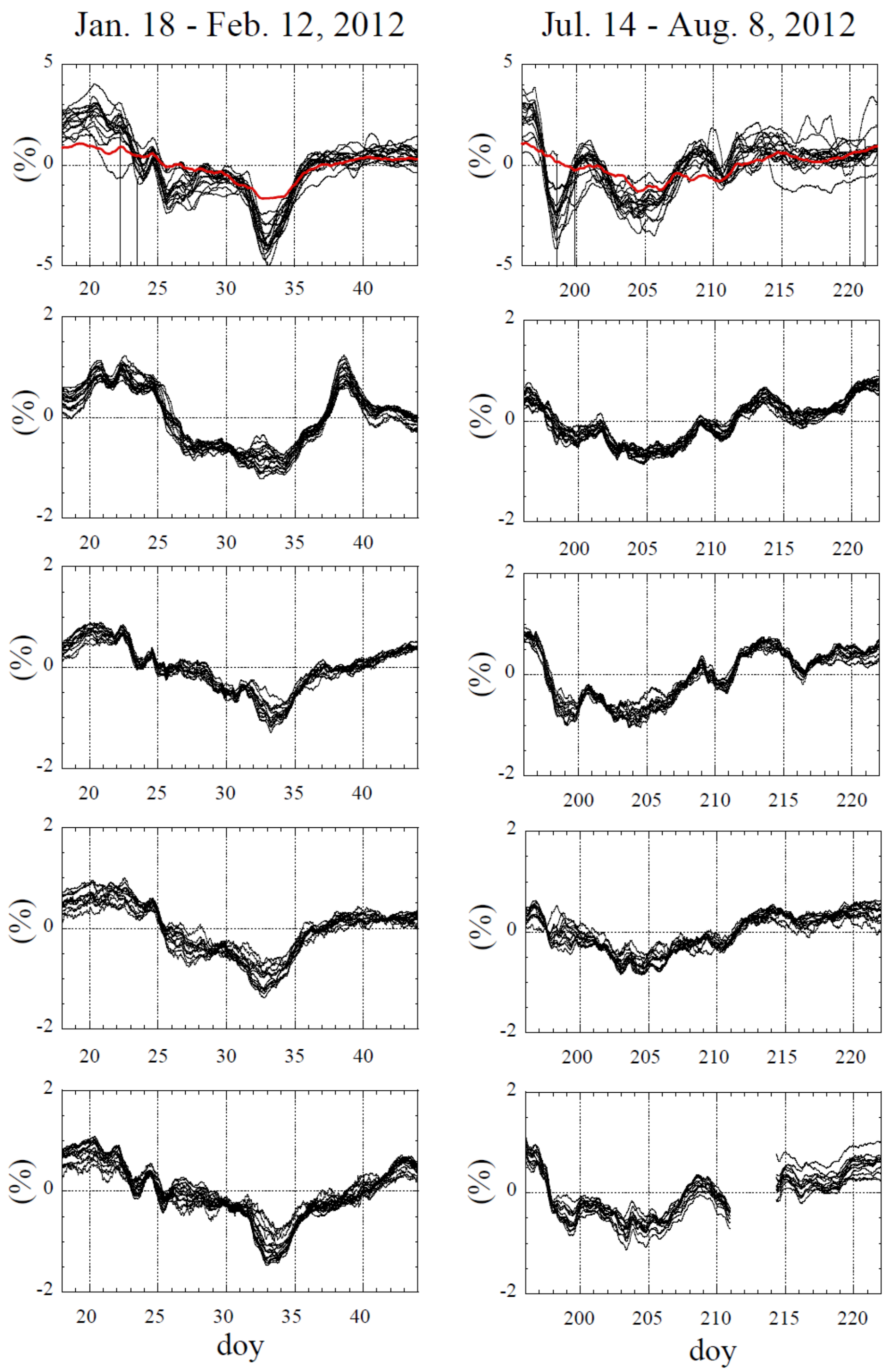

Figure 1. Superposed 24-hour trailing moving averages ($\bar{I}^{obs}_{i,j}(t)$) of hourly count rates observed in January-February, 2012 (left column) and in July-August, 2012 (right column). Top panels show $\bar{I}^{obs}_{i,j}(t)$ of NMs, while the second to bottom panels show $\bar{I}^{obs}_{i,j}(t)$ of all directional channels in Nagoya, Hobart, Kuwait and São Martinho MDs, respectively. The red curve in each top panel displays $\bar{I}^{obs}_{i,j}(t)$ of the PSNM at highest P_c in Table 1.

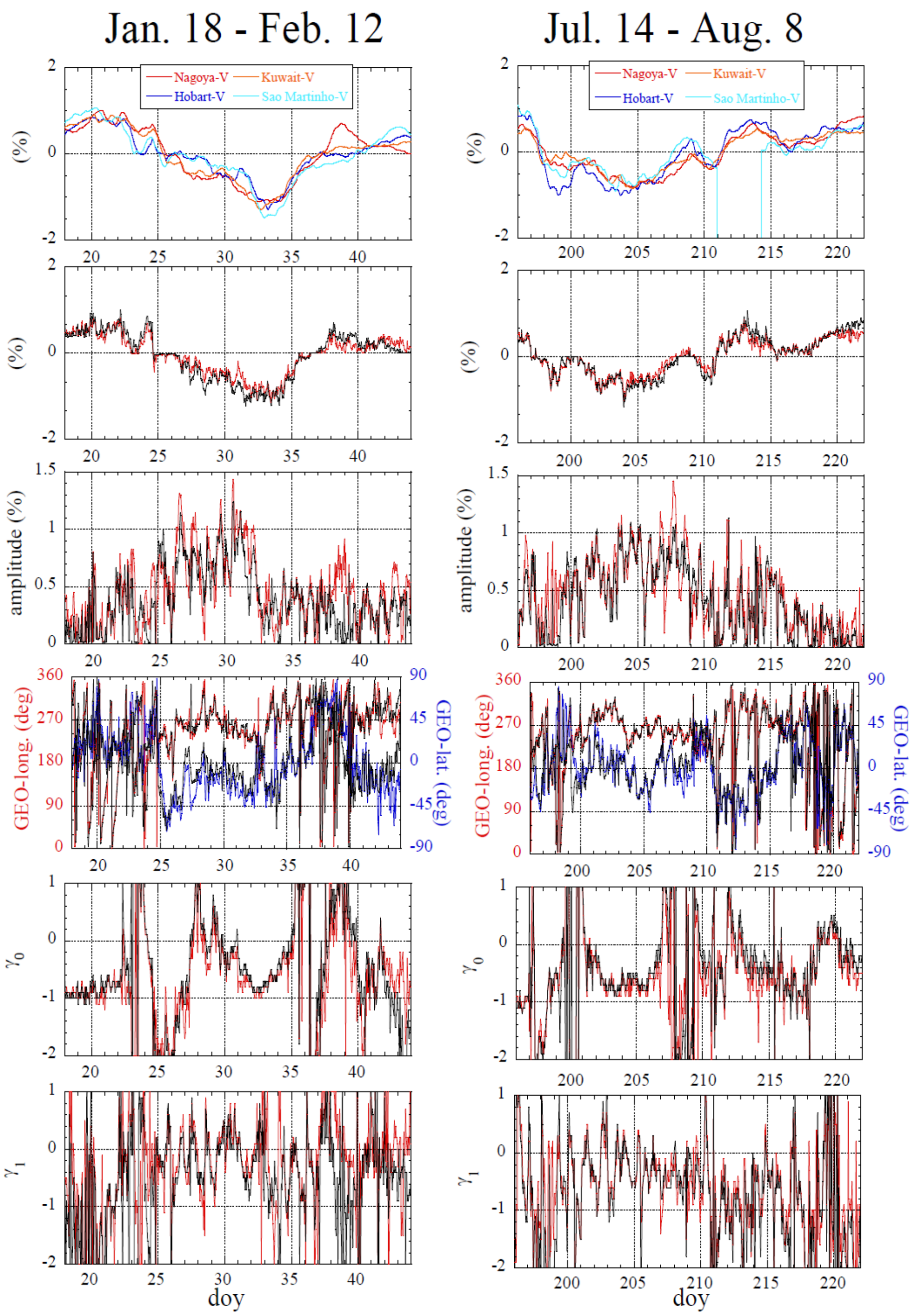

Figure 2. The 24-hour trailing moving averages ($\bar{I}_{i,j}^{obs}(t)$) of four vertical channels in the GMDN (top panels) and the best-fit parameters at 65 GV. From the second to the bottom, each panel shows, the best-fit density, amplitude of the first-order anisotropy, GEO-longitude and latitude of the first-order anisotropy, the power-law indices of the density ($\gamma_0(t)$) and the first-order anisotropy ($\gamma_1(t)$). All red curves and two blue curves in the fourth panels display parameters obtained from best-fitting to the original $I_{i,j}^{obs}(t)$, while black curves display parameters obtained from best-fitting to the normalized $i_{i,j}^{obs}(t)$ of MD data (see text).

($\sqrt{(\xi_1^{0\,c}(t))^2 + (\xi_1^{1\,c}(t))^2 + (\xi_1^{1\,s}(t))^2}$), the GEO-longitude and latitude of the orientation of the diurnal anisotropy, $\gamma_0(t)$, and $\gamma_1(t)$.

We note significant 24-hour variations in the diurnal anisotropy at 65 GV displayed by red and blue curves in the third and fifth panels during several-days periods, when $\bar{I}_{i,1}^{obs}(t)$ in the top two panels shows significant difference between four vertical channels. This is due to the best-fit calculation resulting in the spurious anisotropy directing from the viewing direction of higher count rate detectors, which rotates in space according to Earth's spin.

In order to suppress the difference between MDs causing the spurious anisotropy, we use instead of $I_{i,j}^{obs}(t)$ for MD data in the best-fitting the count rate ($i_{i,j}^{obs}(t)$) normalized to $\bar{I}_{1,1}^{obs}(t)$, i.e. the 24-hour TMA of Nagoya vertical channel, defined as

$$i_{i,j}^{obs}(t) = I_{i,j}^{obs}(t)\bar{I}_{1,1}^{obs}(t)/\bar{I}_{i,j}^{obs}(t).$$

We use $I_{i,j}^{obs}(t)$ for NM data. The best-fit parameters derived from best-fitting to $i_{i,j}^{obs}(t)$ for MD data are displayed by black curves in the bottom five panels of Figure 2. It is seen that the 24-hour variations in the diurnal anisotopy at 65 GV are suppressed in the third panels. The best-fit parameters in Figure 2 are discussed in comparison with the solar wind parameters in other work we presented at this conference [8].

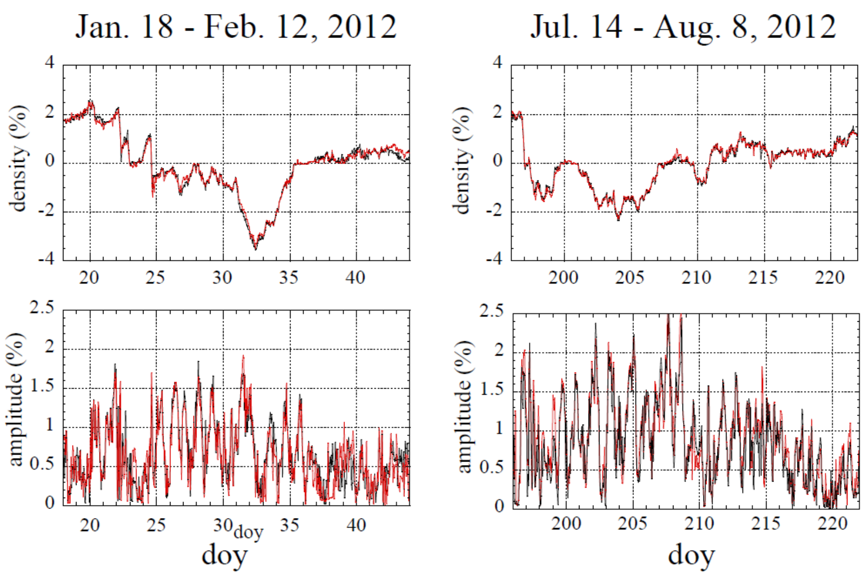

Figure 3. The best-fit density (upper panels) and the amplitude of the first-order anisotropy (lower panels) at 15 GV. Red curves display parameters obtained from best-fitting to the original $I_{i,j}^{obs}(t)$, while black curves display parameters obtained from best-fitting to the normalized $i_{i,j}^{obs}(t)$ of MD data (see text).

As shown in bottom panels in Figure 3, on the other hand, more prominent 24-hour variations are also seen in the diurnal anisotropy at 15 GV monitored by NMs, indicating significant local effects in NM data. This is also responsible for 24-hour variations of the anisotropy orientation and $\gamma_1(t)$ seen in red and blue curves in the fourth and the bottom panels of Figure 2. Although we currently have no good idea to eliminate the effect in NM data, it might be giving a hint that no significant influence of the local effect is seen in the best-fit density and $\gamma_0(t)$ in Figures 2 and 3. We will further develop analysis method with which we can derive the best-fit parameters minimizing the influences from the local effect.

Acknowledgement

This work is supported by the Institute for Space-Earth Environmental Research (ISEE), Nagoya University, the Institute for Cosmic Ray Research (ICRR), University of Tokyo, and the "Strategic Research Projects" grant from ROIS (Research Organization of Information and Systems) in Japan. The observations with the GMDN are supported by Nagoya University with the Nagoya muon detector, by INPE and UFSM with the São Martinho da Serra muon detector, by the Australian Antarctic Division with the Hobart muon detector, and by project SP01/09 of the Research Administration of Kuwait University with the Kuwait City muon detector. N. J. S. thanks the Brazilian Agency- CNPq for the fellowship under grant number 300886/2016-0. EE would like to thank Brazilian funding agencies for research grants FAPESP (2018/21657-1) and CNPq (pQ-301883/2019-0). M. Rockenbach thanks the Brazilian Agency - CNPq for the fellowship under grant number 306995/2021-2. ADL thanks CNPq for grant 309916/2018-6. PSNM maintenance was also supported by Achara Seripienlert and the National Astronomical Research Institute of Thailand. We acknowledge the NMDB database (http://www01.nmdb.eu/), founded under the European Union's FP7 program (contact no. 213007) for providing data. We also gratefully acknowledge the NOAA Air Resources Laboratory (ARL) for the provision of GDAS data, which are available at the READY website (http://www.ready.noaa.gov) and used in this paper. The OMNIWeb dataset of the solar wind and IMF parameters is provided by the Goddard Space Flight Center, NASA, USA.

References

[1] Belov, A. V., et al., *Solar Phys.*, **293**, 68 (2018) [doi:10.1007/s11207-018-1277-6].
[2] Rockenbach, M., et al., *Space Sci. Rev.*, **182**,1 (2014), [doi:10.1007/s11214-014-0048-4].
[3] Buatthaisong et al., *Astrophys. J.*, **939**, 99, (2022), [doi:10.3847/1538-4357/ac96ea].
[4] GMDN collaboration, Global Muon Detector Network (GMDN) data, http://hdl.handle.net/10091/0002001448
[5] Mendonça, R. R. S., et al., *Astrophys. J.*, **830**, 88 (2016). [doi:10.3847/0004-637X/830/2/88].
[6] Munakata, K., et al., *Astrophys. J.*, **938**, 30 (2022), [doi:10.3847/1538-4357/ac91c5].
[7] Kato et al., *JSWSC*, **11**, 31 (2021), [doi:10.1051/swsc/2021005].
[8] Hayashi et al., Pos(ICRC2023)1267, (2023) in this conference.